An Estimation Method of Surface Defects of LMJ Microshells

V. Dutto, A. Choux, Francesca Chittaro, Eric Busvelle, J.-P. Gauthier

An estimation method of surface defects of LMJ microshells

V. Dutto,[a,b] A. Choux,[a] F. C. Chittaro,[b] É. Busvelle,[*,b] and J.-P. Gauthier[b]

[a] *CEA DAM, Centre de Valduc, 21120 Is sur Tille, France*

[b] *Université de Toulon, Aix Marseille Univ, CNRS, LIS, Marseille, France*

[*]Email: busvelle@univ-tln.fr

Number of pages: 31
Number of tables: 2
Number of figures: 13

Abstract

This article presents the development of a radiographic characterization method for microshells. In the LMJ (Laser MegaJoule) framework, microshells are tiny plastic spheres used in inertial fusion laser experiments. For this work, these microshells were characterized using low energy radiography. In the microshell radiographs, phase contrast was noted at the edges of the microshells. The origin of this phenomenon has been identified as sharp variation of gray scale amplitude due to refraction. Our theoretical model links pixel information with microshell geometry and is used for contour detection and characterization. Finally, an estimation of surface defects described by spherical harmonics is calculated.

Keywords — X-rays radiography, Geometrical optics, Image processing, Inverse problem

I. INTRODUCTION

In this paper, we developed a non-destructive characterization method of surface defects of tiny microshells. These microshells are the targets of LMJ, involved in experiments in the field of inertial fusion technology. These targets have stringent constraints for their roughness and sphericity [1, 2].

The method we propose in this paper is based on X-ray radiography. Indeed, shadowgraphy-based techniques have already been applied to such problems (see for instance [3] and references within), but, due to reflection and absorption phenomena, they give little information about the interior of the microshell wall. On the other hand, since the material composing the microshells is weakly X-ray absorbing and reflecting, the radiographs are more adapted to inspect the interior wall of the microshell. However, on the microshell radiographs, another phenomenon, besides absorption or reflection, is observed : phase contrast. In this paper, we will show that the origin of this phenomenon has been identified as sharp variation of amplitude due to refraction at the inner and outer surface of the shell.

To characterize these microshells, several techniques based on X-rays, including tomography, are commonly used [4–6]. In this paper, we are more concerned with sample throughput, in order to speed-up the characterization process.

Indeed, a complete tomograpic image usually takes few days to be accomplish and process. A half a day is needed for image acquisition due to large number of radiographs needed to reconstruct the whole microshell surface and adequately capture the low mode features. Several more hours (i.e. 1-2 days) is often needed to post-process the tomographic image. The proposed method consists of taking several X-ray radiographs of the sphere, from different viewpoints. The acquisition and processing time by this method is less than two hours.

To establish a link between the microshell surface and the radiographs, here we propose a model of the propagation of the X-rays through the plastic sphere based on geometrical optics. This model allows us to detect the contour of the microshell, as they are closely related to the inflection points of the intensity profile detected by the detector [7, 8]. More precisely, locating some inflection points allows us to recover the edge of the sphere. Additionally, this model is able to recover quantitatively the phase and absorption contrast observed in the radiographs.

The microshell deviations from a perfect sphere is considered a defect and can be described by

spherical harmonics, that is, the disturbances of the nominal radius is developed in the orthonormal basis defined by them (see [9, 10] for instance). Spherical harmonics coefficients are computed by the least squares estimation method. In this paper, we focus on the application of our radiographic method to low deformation modes (that is, for instance, flattening, decentering, form defects), and not on high ones (texture). Indeed, we want to reconstruct an object using a minimal number of radiographic views. Following the classification in [11] concerning data insufficiency in computed tomography, we are concerned with the first approach of this classification: interpolation of missing data thanks to spherical harmonics. Therefore, we will see in this paper that only low mode issues can be estimated. The results obtained by our method allow the microshell surface defects characterization with a micrometric accuracy.

The structure of the paper is the following: in section II, the coherence of the radiographic system is studied. In section III, a model is elaborated using geometrical optics. In section IV, a method to estimate the surface disturbance is developed. The method is applied and validated in section V. In section VI, the uncertainty of surface disturbance measurement is given.

II. COHERENCE

The following section is dedicated to the system coherence which affects our study.

In our experimental set up, a micrometric source emits a poly-chromatic X-ray and a detector is at a distance of 0.4 m from the source with a pixel size of 55 μm. The temporal coherence length is:

$$L_c = \frac{v}{\Delta\nu},$$

with:

- v, the wave speed, here equivalent to the speed of light $v \simeq c = 3 \times 10^8 m/s$;
- $\Delta\nu$, the spectral width.

The main energies of the generator are the L spectral lines of tungsten (Energies: 8, 9, and 11.6 keV). Between 8 and 11.6 keV, $\Delta\nu = 8.7 \times 10^{17}$ Hz. $L_c = 3.5 \times 10^{-10}$ m which is smaller than our distance d between the source and the sensor ($d = 0.4$ m). Therefore, the temporal coherence is not sufficient to have interference.

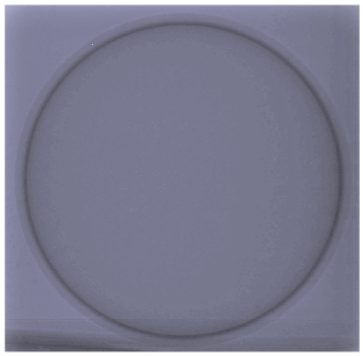

Fig. 1. Radiograph of a typical capsule

The spatial coherence length is:

$$L_s = \frac{\lambda d}{\Delta S},$$

with:

- λ, the wave length;
- ΔS, the source width.

For the energy 11.6 keV, $\lambda = 1.07 \times 10^{-10}\ m$. The source width is about 7×10^{-6} m. $L_s = 6.11 \times 10^{-6}$ m which is smaller than the pixel size (55 μm). Here, we can also conclude that the spatial coherence is not sufficient to cause interference.

Thus, the coherence needed to obtain interference is not reached. We conclude that phase contrast is created by an amplitude variation from refraction. The wave optics can model refraction in capsule [12] but in this paper we will present a common model based on the geometrical optics.

III. GEOMETRICAL OPTICS

III.A. Theory

In this section, a simulated microshell radiography is used. The propagation of light rays is computed by using the coordinates chosen in [3, 13], that we will briefly cover here. The wave phenomena of the light are not taken into account in this paper. For an insight on these issues, see [12].

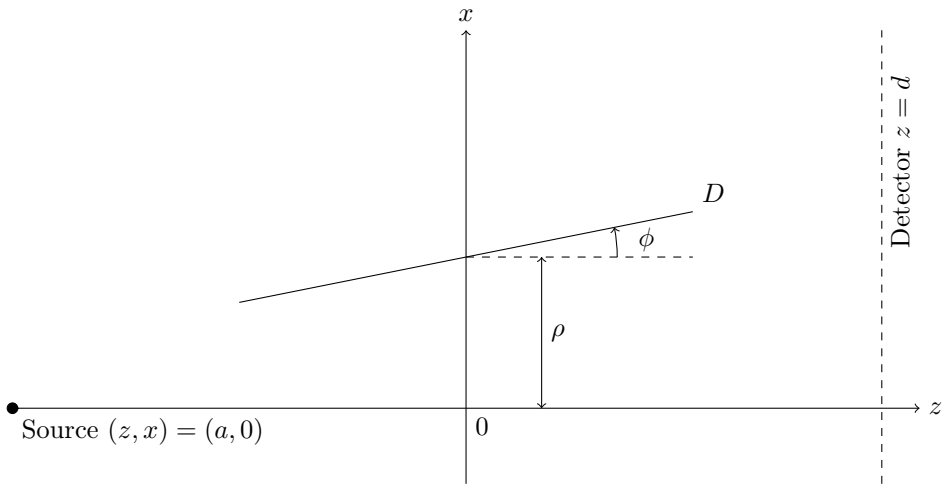

Fig. 2. Lines configuration

III.A.1. General case

Since we are going to proceed by small variations around the ideal case, let us first consider a perfect sphere. Let (z, x, y) be an orthogonal frame centered in the sphere center. Let z be the optical axis, oriented from the source to the sensor. There is a radial symmetry around this axis so we will only consider the plane (z, x). In this plane, the source lies in the point $(-a, 0)$ and the sensor is the vertical line $z = d$.

Straight lines are parameterized by ρ and φ, where ρ is the x-intercept and φ the angle between the z-axis and the line (see Figure 2), then the equation of a straight line is $x = z\tan(\varphi)+\rho$. This parametrization is well adapted to the geometry of our system, although it does not describe vertical lines; these lines being orthogonal to z-axes, play no role in our model. The lines passing through the source are described by the relation $\rho = a\ \tan(\varphi)$.

Refraction is the deviation of the light rays when they change their medium of propagation. Let S be a surface and $\mathbf{n}$ be the normal vector to this surface. Let us denote α the angle between an incident ray and $\mathbf{n}$, and α' the angle between the corresponding refracted ray and $-\mathbf{n}$. We denote n the complex refractive index of the medium where is the incident ray (with $\Re(n) = \gamma$ and $\Im(n) = \beta$), and n' the refractive index of the medium of the refracted ray (with $\Re(n') = \gamma'$ and $\Im(n') = \beta'$). While these refractive indices depend on wavelength λ, the dependence to the

wavelength is omitted for now[a]. The Snell-Descartes law relates these quantities as follows:

$$\gamma \sin \alpha = \gamma' \sin \alpha' \tag{1}$$

We write (1) in the coordinates proposed by Choux (cf. [13, lemma 14 and 17]). Let S_i be the i^{th} interface a ray crosses; the incident ray is characterized by the parameters (ρ_i, φ_i), the outgoing one by $(\rho_{i+1}, \varphi_{i+1})$. ρ_i and ρ_{i+1} are linked by the relation:

$$\rho_{i+1} = \frac{\gamma \rho_i \cos \varphi_i}{\gamma' \cos(\varphi_{i+1})}$$

The relation between φ_i and φ_{i+1} depends on the direction of the ray with respect to the center of the sphere. If the ray is incoming the sphere (that is, if it is approaching to its center) then:

$$\varphi_{i+1} = \varphi_i - \arcsin\left(\frac{\rho_i \cos(\varphi_i)}{r}\right) + \arcsin\left(\frac{\gamma \rho_i \cos(\varphi_i)}{\gamma' r}\right), \tag{2}$$

while when the ray is exiting the sphere then:

$$\varphi_{i+1} = \varphi_i + \arcsin\left(\frac{\rho_i \cos(\varphi_i)}{r}\right) - \arcsin\left(\frac{\gamma \rho_i \cos(\varphi_i)}{\gamma' r}\right). \tag{3}$$

There are two refractions by interface, one upon entering and the other exiting the microshell. The gas inside the microshell is assumed to be air. Each outgoing ray is refracted by one or more interfaces. The number of crossed interfaces depends on the angle of the outgoing ray.

In order to determine the transmitted and reflective energy, the Fresnel coefficients are computed. The wall of the microshell is plastic, which is not magnetic nor conductive. For transmission (Tra) and reflection (Ref) the Fresnel laws are:

$$Tra = \frac{2\gamma \cos(\theta)}{\gamma \cos(\theta) + \gamma' \cos(\theta')} \tag{4}$$

$$Ref = \frac{\gamma \cos(\theta) - \gamma' \cos(\theta')}{\gamma \cos(\theta) + \gamma' \cos(\theta')} \tag{5}$$

where

[a] A way to incorporate polychromatic spectrum into model is to superimpose simulation obtained for different energies. The result stays a good approximation if the energy band is not too large.

- θ is the incident angle in $]0, \frac{\pi}{2}[$;
- θ' is the refracted angle;
- γ and γ' are the real part of the refractive index respectively in incident and refracting medium.

The absorption in a medium follows the Beer-Lambert law. Let X be the distance covered by a ray in an absorbing medium of refractive index $n(\lambda) = \gamma(\lambda) + i\beta(\lambda)$, and let I be the intensity of ray before absorption and I_{abs} be the intensity after absorption. The Beer-Lambert law is:

$$I_{abs} = I \ e^{-\frac{4\pi\beta(\lambda)}{\lambda}X} \tag{6}$$

III.A.2. Full ball case

We develop a model based on geometrical optics. In order to illustrate our approach, we will first consider a full plastic ball of radius R. In this case, equations are easy to state and to solve explicitly. The refractive index of air is 1 and the refractive index of the ball is denoted $n' \in \mathbb{C}$.

The emitted rays are parameterized by,

$$\rho_0 = a \ \tan\varphi_0,$$

and their intensity is set arbitrarily to $I_1 = 1$.

For an outgoing ray, there are two possibilities:

1. if $\varphi_0 < \arcsin\frac{R}{a}$, then the ray intersect the ball and is subject to refraction, reflection and absorption,
2. if $\varphi_0 > \arcsin\frac{R}{a}$, then the ray does not goes across the ball and it keeps its linear propagation until it reaches the sensor.

If the ray goes across the ball, its directions and absorption are computed. The first refraction is an incoming one. It is computed thanks to (2):

$$\rho_1 = \frac{\rho_0\cos\varphi_0}{\gamma'\cos\varphi_1} \tag{7}$$

$$\varphi_1 = \varphi_0 - \arcsin\frac{\rho_0\cos\varphi_0}{R} + \arcsin\frac{\rho_0\cos\varphi_0}{\gamma' R} \tag{8}$$

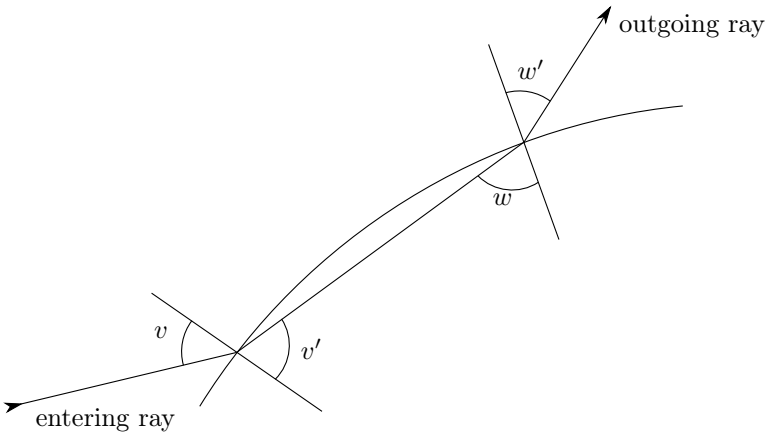

Fig. 3. Angles notations

The ray undergoes a refraction when exiting the ball. Following (3), we obtain:

$$\rho_2 = \frac{\gamma' \rho_1 \cos\varphi_1}{\cos\varphi_2} \tag{9}$$

$$\varphi_2 = \varphi_1 + \arcsin\frac{\rho_1 \cos\varphi_1}{R} - \arcsin\frac{\gamma' \rho_1 \cos\varphi_1}{R} \tag{10}$$

By replacing (7) and (8) into (9) and (10), we obtain:

$$\begin{aligned}\rho_2 =& \rho_0 \frac{\cos\varphi_0}{\cos\varphi_2} \\ \varphi_2 =& \varphi_0 + 2\left(\arcsin\frac{\rho_0 \cos\varphi_0}{\gamma' R} - \arcsin\frac{\rho_0 \cos\varphi_0}{R}\right)\end{aligned}$$

Due to the absorption, the intensity of the ray decreases when passing through the ball. The distance X covered being $X = 2\sqrt{R^2 - (\rho_2 \cos(\varphi_2))^2}$, the intensity of the outgoing ray is given by (6). The outgoing ray propagates until it reaches the detector, that is, up to the vertical line $z = d$

The intensity of the refracted wave is computed by the Fresnel coefficients. Let v, v', w, w' be the angles showed in Figure 3, where $v' = w$ and $w' = v$. The following relations express the

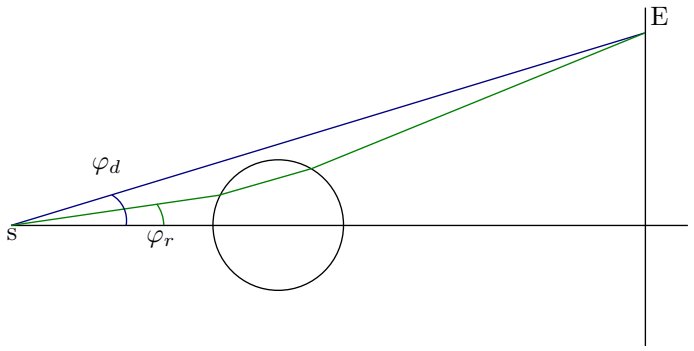

Fig. 4. Two rays arriving to the same sensor point, a direct and a refracted.

angles v, v', w, w' in function of the refractive angles:

$$\begin{aligned}
\sin v &= \rho_0 \frac{\sin\left(\frac{\pi}{2} - \varphi_0\right)}{R} = \rho_0 \frac{\cos\varphi_0}{R} \\
\sin v' &= \rho_1 \frac{\cos\varphi_1}{R} \\
\sin w &= -\rho_1 \frac{\sin\left(\frac{\pi}{2} + \varphi_1\right)}{R} = -\rho_1 \frac{\cos\varphi_1}{R} \\
\sin w' &= \rho_2 \frac{\sin\left(\frac{\pi}{2} + \varphi_2\right)}{R} = -\rho_2 \frac{\cos\varphi_2}{R}
\end{aligned}$$

The Fresnel coefficients are obtained thanks to (5). For the first refraction we have:

$$\begin{aligned}
Ref_1 &= \frac{\cos v - \gamma' \cos v'}{\cos v + \gamma' \cos v'} \\
&= \frac{\sqrt{R^2 - \rho_0^2 \cos^2\varphi_0} - \sqrt{\gamma'^2 R^2 - \rho_0^2 \cos^2\varphi_0}}{\sqrt{R^2 - \rho_0^2 \cos^2\varphi_0} + \sqrt{\gamma'^2 R^2 - \rho_0^2 \cos^2\varphi_0}},
\end{aligned}$$

and similarly for the second refraction:

$$Ref_2 = \frac{\sqrt{\gamma' R^2 - \rho_0^2 \cos^2\varphi_0} - \sqrt{R^2 - \rho_0^2 \cos^2\varphi_0}}{\sqrt{\gamma' R^2 - \rho_0^2 \cos^2\varphi_0} + \sqrt{R^2 - \rho_0^2 \cos^2\varphi_0}}.$$

Finally, the theoretical profile is obtained by these geometrical computation. It is proportional to the intensity of the X-rays impinging upon the detector. Every point of the detector may be reached by a maximum of two rays[b], one direct with an angle φ_d and another refracted with an angle φ_r (see Figure 4).

We denote respectively $p_d(\varphi_d)$ and $p_r(\varphi_r)$, the intensity of a refracted ray and the intensity

[b] the reflected rays are neglected

of an absorbed ray. By convention, when the outgoing ray with the angle φ reaches the sensor directly (respectively when it is refracted), the intensity of this ray is set to $p_r(\varphi) = 0$ (respectively $p_d(\varphi) = 0$).

The received power on a little 1D element $[x, x + dx]$ coming from direct rays emitted with the angles $[\varphi_d, \varphi_d + d\varphi_d]$ and the refracted rays emitted with the angles $[\varphi_r, \varphi_r + d\varphi_r]$ is:

$$P_{[x,x+dx]} = \int_{\varphi_d}^{\varphi_d+d\varphi_d} p_d(\varphi)d\varphi + \int_{\varphi_r}^{\varphi_r+d\varphi_r} p_r(\varphi)d\varphi$$

Let $x = f_d(\varphi)$ (respectively $x = f_r(\varphi)$) be the final point of a direct ray (respectively refracted) emitted with the angle φ. In the two integrals, by writting $x = f(\varphi)$, $d\varphi = \frac{1}{f'(f^{-1}(x))}$, the coordinates change is applied:

$$P_{[x,x+dx]} = \int_{x}^{x+dx} \frac{p_d(f_d^{-1}(x))}{f_d'(f_d^{-1}(x))}dx + \int_{x}^{x+dx} \frac{p_r(f_r^{-1}(x))}{f_r'(f_r^{-1}(x))}dx,$$

so that we can compute the intensity received in x:

$$p(x) = \frac{p_d(f_d^{-1}(x))}{f_d'(f_d^{-1}(x))} + \frac{p_r(f_r^{-1}(x))}{f_r'(f_r^{-1}(x))}.$$

This intensity is the sum of two functions. The first has a discontinuity at $\bar{x}$ point defined by the line from the S source and microshell's tangent. The second function is continuous. So p_x is discontinuous in $\bar{x}$.

III.B. Simulations

III.B.1. Plastic microshell

From now on, we will consider a hollow sphere. In this section, we simulate a microshell radiograph, where the microshell is a refracting and absorbing ball, with refractive index $n' = 1 - 8 \times 10^{-7} + i\ 1.3 \times 10^{-9}$. This value is chosen in data [14] for plastic with a 10 keV energy (in agreement with the experimental parameters), and has been adapted during simulation to fit the experimental results (because the density of plastic is unknown).

To perform the simulations, we used the following parameters:

- a ball with a radius of 722 μm;

- the distance source-center of the ball equal to $1,5\ cm$;
- the distance source-sensor equal to $40\ cm$;
- the pixel size equal to $55\ \mu m$ (therefore, we have a zoom of about $30\times$).

An experimental profile obtained with a plastic ball with a radius of $722\ \mu m$ is compared to a simulated profile. The support is a plastic membrane which is weakly X-ray absorbing.

If $\varphi < \arcsin \frac{R}{a}$, this ray is refracted a first time when entering the microshell and a second time when it leaves the microshell. At the exit of the microshell, the ray has been deviated and the angle between this ray and (Oz) is φ' which is superior to φ. The ray parallel to (Oz) is not deviated, and when $\varphi \longrightarrow \arcsin \frac{R}{a}$, the refracted rays are increasingly refracted.

This fact is observed on the Figure 5. In abscissa, we plot the distance of the point in the sensor from $(d, 0)$; the blue dashed line shows the refracted power, and the red solid line the direct power. The refracted power is non-zero for distances less than $22.5\ mm$, while the direct power is non-zero and almost constant for distances greater than $20\ mm$ and lower than $25\ mm$. In particular, in the interval $[20\ mm, 22.5\ mm]$, the sensor receives contributions both from the refracted and direct wave.

The result is shown on Figure 6(a). We observe that the absorption of the simulated curve (red) is similar to the experimental profile (blue). The difference of absorption from pixel 1 to pixel 130 is due to the plastic membrane alveolus[c]. The main difference between the two profiles is at the interface: a peak linked to the phase contrast is present, but this peak has a superior amplitude compared to the peak in the experimental profile. Moreover, the peak of the experimental profile is larger than the simulated peak. These observations are in accordance with the explanations given on the difference between the experimental profile and the simulated one (blur due to non-point source and sensors effects).

On Figure 6(a) the discontinuity corresponding to the microshell shape is clearly visible. In the experimental situation, the profile is not directly measured because the image is "pixelized" and blurred (for many reasons including the fact that the source spot is not a point source, and not monochromatic). To simulate the geometric blur, the theoretical profile $p(x)$ (Figure 6(a)) is convoluted with a function g which represents the acquisition process. g is supposed to be

[c]On this capture, the microshell is compressed between 2 plastic membranes with holes in order to block it in a centered position

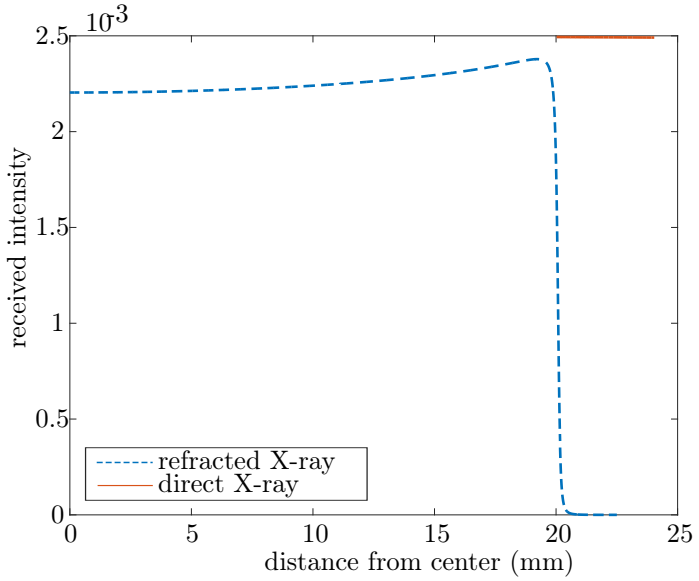

Fig. 5. Refracted rays and direct rays.

a positive convolution kernel with small support in $[-\eta, \eta]$, unimodal and differentiable (like a Gaussian kernel). The derivative of profile after convolution is:

$$\frac{d}{dx} p * g(x) = \int_{-\eta}^{\eta} p(x-t) g'(t) dt.$$

If $p(x)$ is smooth between $x-\eta$ and $x+\eta$, $p(x-t) = p(x) + O(t)$ and so this integral is:

$$p(x) \int_{-\eta}^{\eta} g'(t) dt + \int_{-\eta}^{\eta} O(t) g'(t) dt = O(\eta).$$

On the other hand, if $p(x)$ has a first kind discontinuity at $\bar{x} \in [x-\eta, x+\eta]$, then

$$\begin{aligned} \frac{d}{dx} p * g(x) &= p(\bar{x}^-) \int_{-\eta}^{x-\bar{x}} g'(t) dt + p(\bar{x}^+) \int_{x-\bar{x}}^{\eta} g'(t) dt + O(\eta) \\ &= \left[p(\bar{x}^-) - p(\bar{x}^+) \right] g(x-\bar{x}) + O(\eta), \end{aligned}$$

where $p(\bar{x}^-) = \lim_{x \to \bar{x}^-} p(x)$ and $p(\bar{x}^+) = \lim_{x \to \bar{x}^+} p(x)$. The second derivative at $\bar{x}$ is null and changes its sign. Thus, a discontinuity of the theoretical intensity profile corresponds, on the blurred profile, to an inflection point.

The standard deviation is chosen to be equal to the pixel size, e.g. 2×10^{-7} m. Results in

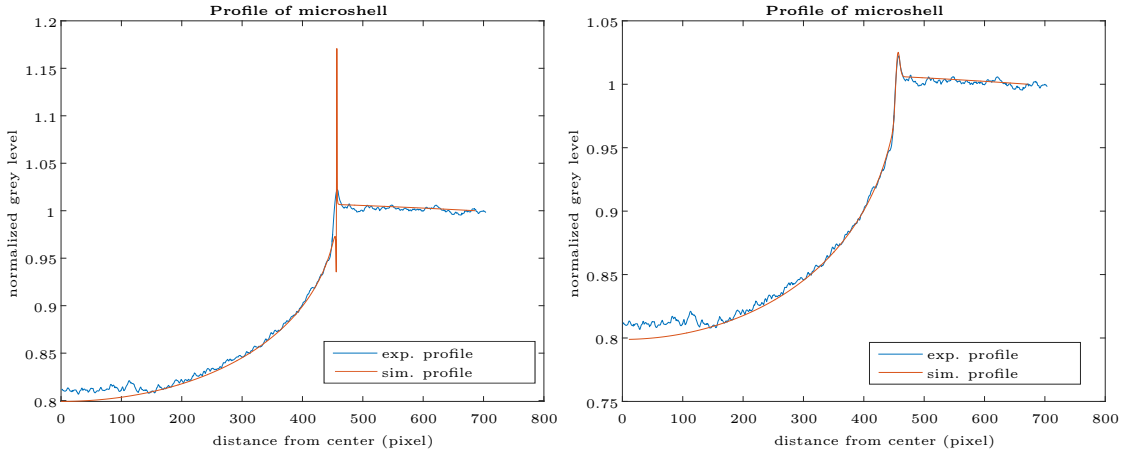

(a) Without blur. (b) With blur.

Fig. 6. Profile, for a microshell of $R_{ext} = 722\ \mu m$ outer radius and with refractive index $n' = 1 - 8 \times 10^{-7} + i\ 1.3 \times 10^{-9}$, experimental and simulated by model of refraction and absorption.

figure 6(b) indicate that the simulated curve is very similar to the experimental curve. The mean error between the two curves is 0.6% and the maximum error is 5%.

Moreover, we compare the two profiles: one in which we also model the reflection (using the Fresnel coefficients), and one in which we do not. As the two curves are in agreement, with a local maximal variation of 0.1%, the intensity variation as a function of the incident angle is neglected. This is justified by the fact that the reflection is neglected, because it contributes to 0.1% of the theoretical profile.

We can conclude that the model based on geometrical optics gives good results and that information of great interest can be extracted from the experimental curves.

Indeed, the inflection point in the experimental profile corresponds exactly to the discontinuity, i.e. the place where the X-rays are tangent to the surface of the sphere. Therefore, from the location of the inflection point we can deduce the radius of the sphere.

Figure 7 shows the second derivatives of the profiles, experimental and simulated, from curves of Figure 6(b). On Figure 7, the position of the computed interface is plotted by the black vertical line. The second derivatives of the profiles, on the experimental (blue) and on the simulated (red), are superposed. We note that the vertical line crosses the curves when they are between a minimum at pixel 455 and a maximum at pixel 460. Between these two values, the curves change their sign which defines an inflection point.

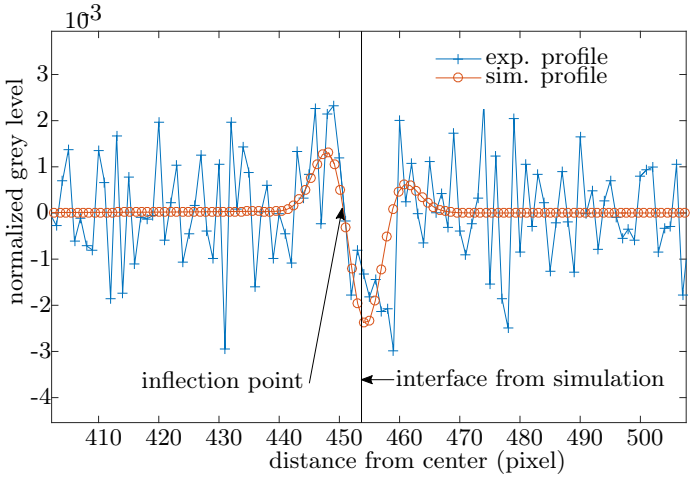

Fig. 7. Second derivatives of experimental and simulated profiles of a microshell with an outer radius $R_{ext} = 722\ \mu m$ of and a refractive index of $n' = 1 - 8.10^{-7} + 1,3.10^{-9}$.

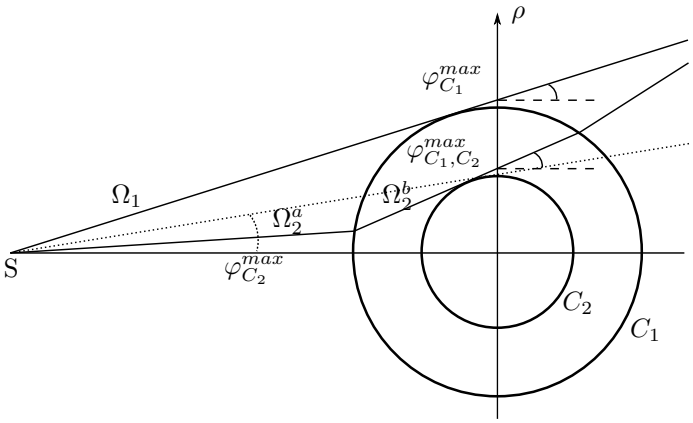

Fig. 8. Maximal angles $\varphi_{C_1}^{max}$,$\varphi_{C_2}^{max}$ and φ_{C_1,C_2}^{max} of each thickness delimited by their shapes C_1 and C_2

III.B.2. Numerical example

We now simulate a microshell of radius 722 μm and thickness 122 μm. The detector is positioned at 40 cm from the source, the microshell center is at 1 cm from the source.

We denote by C_1 the external surface of the microshell, and by C_2 the interface between the two layers. Ω_1 is the ray tangent to C_1; the ray Ω_2 emitted by the source and tangent to C_2 is composed by three parts: the Ω_2^a ray, emanating from the source, the Ω_2^b ray, the refraction of Ω_2 when it passes through C_1 (see Figure 8), Ω_2^c the ray leaving the sphere and crossing the sensor.

Let $\varphi_{C_1}^{max}$, $\varphi_{C_2}^{max}$ and φ_{C_1,C_2}^{max} be respectively, the angle of Ω_1, the angle of Ω_2 and the angle of Ω_2^b.

Let x be the distance between the center and a point of the detector. For each ray, the distance x at their arrival on the detector is computed. The Ω_1 rays are not refracted, the Ω_2 rays are refracted twice (incoming and outgoing refraction).

The tangent ray is found numerically as the maximum ray refracted by C_1 and not refracted by C_2 corresponding to the maximum angle φ_{C_2}.

The intersection of Ω_1 with the sensor, is located at $x = 2.888\ cm$; the tangent ray to C_2 (without refraction) is located at $x = 2.4\ cm$.

The position of the ray that tangents the second interface, refracted by the first surface, entering and exiting the microshell, is imaged on the detector. The deviation is then the difference of the position of this ray with the position of the tangent ray to C_2 (without refraction). For a refractive index of $n = 1 - 8.10^{-7}$, the deviation of the second interface is $0.01\ cm$. For a stronger refraction index of $n = 1 - 5.10^{-6}$, the deviation of the second interface is $0.04\ cm$. For a lower refraction index of $n = 1 - 5.10^{-7}$, the deviation of the second interface is close to 0 (up to the numerical accuracy).

Since the detector has a pixel size of $55\ \mu m$, depending on the refraction index, this variation can change the position of the interface on the sensor.

This variation and the geometric blur must be weak in order to have a correct approximation achieved by the use of geometrical optics. The hypothesis of a very weak diffraction, stated to apply the geometrical optics, may not be accurate. Indeed, the diffraction can slightly modify the values obtained experimentally. Moreover, the results obtained depend on several parameters, including the refractive index. The refractive index is estimated from the experimental data because the microshell composition is unknown. It is possible that the estimated refractive index is slightly different from the experimental refractive index (the X-ray beam does have a bandwidth which will have a slightly varying refractive index over the wavelengths).

IV. SURFACE DISTURBANCE

IV.A. Theory

The surface of the microshell can be described as a deformed sphere. In spherical coordinates, a perfect sphere of radius R is determined by the equation $\rho(\theta, \varphi) = R$, where $\varphi \in [0, 2\pi]$ and

$\theta \in [0, \pi]$. We recall that the relation between spherical and Cartesian coordinates is:

$$x = \rho(\theta, \varphi) \sin\theta \cos\varphi,$$
$$y = \rho(\theta, \varphi) \sin\theta \sin\varphi,$$
$$z = \rho(\theta, \varphi) \cos\theta.$$

For a sphere deformed by a small perturbation, this equation becomes:

$$\rho(\theta, \varphi) = R + \varepsilon(\theta, \varphi) \tag{11}$$

where $\varepsilon(\theta, \varphi)$ represents the small radial deformation around R in (θ, φ). The $\varepsilon(\theta, \varphi)$ deformation can be developed in a series of spherical harmonics [15, Chapter 1, page 14]:

$$\varepsilon(\theta, \varphi) = \sum_{l=0}^{\infty} \sum_{m=-l}^{l} \lambda_{l,m} Y_l^m(\theta, \varphi) \tag{12}$$

where,

- l is the spherical harmonics mode;
- m is the spherical harmonics order at mode l;
- $Y_l^m(\theta, \varphi) \in \mathbb{R}$ is a normalized real spherical harmonic, defined here below;
- $\lambda_{l,m}$ are the coefficients of the development.

Definition 1 (Spherical harmonic)

For every $l \geq |m|$, the real spherical harmonics are defined as follows (cf. [16]):

- *if $m < 0$,*
$$Y_l^m(\theta, \varphi) = \sqrt{\frac{(2l+1)(l-|m|)!)}{2\pi(l+|m|)!}} P_l^{|m|}(\cos\theta) \sin(|m|\varphi),$$
- *if $m = 0$,*
$$Y_l^0(\theta, \varphi) = \sqrt{\frac{2l+1}{4\pi}} P_l^0(\cos\theta),$$
- *if $m > 0$,*
$$Y_l^m(\theta, \varphi) = \sqrt{\frac{(2l+1)(l-|m|)!)}{2\pi(l+|m|)!}} P_l^{|m|}(\cos\theta) \cos(|m|\varphi)$$

where P_l^m are the associated Legendre polynomial.

The contours of the sphere are discretized, on one hand by the measurement process (because the image is composed of pixels), on other hand by an averaging and interpolating operation that we perform on measured data, in order to reduce the noise level of the pixels. Indeed, knowing the center of a surface of the microshell, the pixels are interpolated to give the gray-scale level depending on its distance to the center. Then the average for a chosen opening angle is computed.

After discretization, equation (11) becomes:

$$\forall (i,j) \in (\mathbb{N} \setminus \{0\})^2 \text{ with } i \leq N \text{ and } j \leq M,$$
$$\rho(\theta_i, \varphi_j) = R + \varepsilon(\theta_i, \varphi_j) \tag{13}$$

where

- N is the number of points on a contour;
- M is the number of radiographs taken from different view angles.

Replacing $\varepsilon(\theta_i, \varphi_j)$ in (13) by its expression (12), the following equation is obtained:

$$\rho(\theta_i, \varphi_j) = R + \sum_{l=0}^{\infty} \sum_{m=-l}^{l} \lambda_{l,m} Y_l^m(\theta_i, \varphi_j). \tag{14}$$

Remark

Being $Y_0^0(\theta_i, \varphi_j)$ constant, the equation (14) can be written as:

$$\rho(\theta_i, \varphi_j) = \tilde{\lambda}_{0,0} Y_0^0 + \sum_{l=1}^{\infty} \sum_{m=-l}^{l} \lambda_{l,m} Y_l^m(\theta_i, \varphi_j).$$

where $R + \lambda_{0,0} Y_0^0 = \left(\frac{R}{Y_0^0} + \lambda_{0,0}\right) Y_0^0 = \tilde{\lambda}_{0,0} Y_0^0$.

The spherical harmonics forming an orthogonal system for the scalar product on $\mathbb{S}^2$ with the measure $\sin\theta d\theta d\varphi$, the equation (14) is easy to solve. The coefficients of spherical harmonics $\lambda_{l,m}$ can be estimated up to order L by orthogonal projection on the basis $(Y_l^m)_{0 \leq |m| \leq l \leq L}$. From the values $\rho(\theta_i, \varphi_j)$ this projection can be computed by using a weighted least squares method. Indeed, the spherical harmonics are described in the spherical coordinates, while the points measured on

the contours are in the Cartesian coordinates. A transformation of the variables from the Cartesian coordinates (z, x, y) to the spherical coordinates (ρ, θ, φ) with $\theta \in [0, \pi]$ and $\varphi \in [0, 2\pi]$ is done in order to apply the least squares method. The Jacobian of the change of variables is equal to $\rho^2 \sin\theta$. A weighting by $\rho^2 \sin\theta$ is then performed to take into account the distribution of the points.

Let T be the vector of the spherical harmonic coefficients:

$$T = \begin{bmatrix} \tilde{\lambda}_{0,0} & \lambda_{1,0} & \lambda_{1,1} & \dots & \lambda_{L,L} \end{bmatrix},$$

and let A be the values of spherical harmonics in each point:

$$A = \begin{bmatrix} Y_0^0 & Y_0^1(\theta_1, \varphi_1) & \dots & Y_L^L(\theta_1, \varphi_1) \\ Y_0^0 & Y_0^1(\theta_1, \varphi_2) & \dots & Y_L^L(\theta_1, \varphi_2) \\ \vdots & \vdots & \ddots & \vdots \\ Y_0^0 & Y_0^1(\theta_N, \varphi_{2M}) & \dots & Y_L^L(\theta_N, \varphi_{2M}) \end{bmatrix},$$

Indeed, a single radiograph gives the points $\rho(\theta_i, \varphi_j)$ and $\rho(\theta_i, \varphi_{M+j})$ where $\varphi_{M+j} = \varphi_j + \pi$.

The relation giving the coefficients of spherical harmonics is:

$$T = (A^t Q A)^{-1} (A^t Q b)$$

where b is the vector of the points which composed the contours, and Q the weighted matrix.

The coefficients of the spherical harmonics are obtained and represent the deformations of the surfaces and the thicknesses. The coefficients characterizing the thickness are equal to the difference of the coefficients modeling the surfaces of this thickness, by linearity of (12).

IV.B. Numerical validation

We now validate the algorithm described in previous section. In order to do so, a microshell with known deformations, described by spherical harmonics (see Figure 9(a)), is simulated. A number M of contours on this microshell is taken, with a uniform rotation pitch $\varphi \in [0, 2\pi]$ around the axis x.

On these contours, we add to the radius an error, distributed by a uniform law in $[-0.01\%, 0.01\%]$.

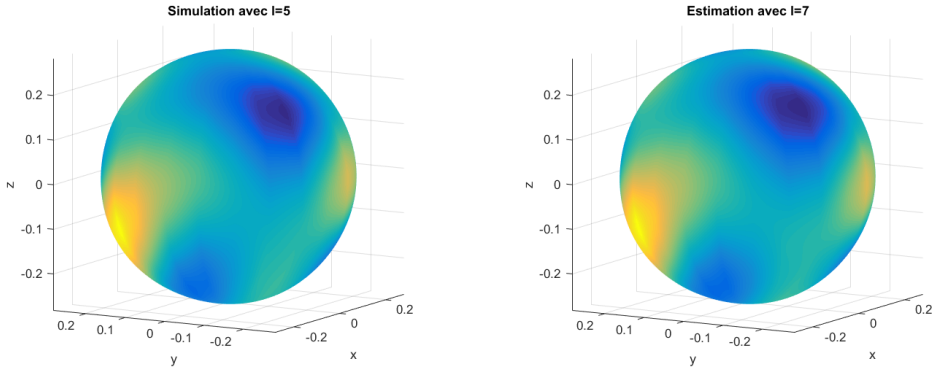

(a) Simulated surface. (b) Estimated surface.

Fig. 9. Estimation for a surface.

The value of 0.01 % corresponds to the typical measurement error for microshells of 1 mm, which is of the order of a micrometer.

From the M contours, the coefficients of the spherical harmonics are estimated (see Figure 9(b)). The error between the coefficient and their estimation is computed.

This operation is repeated for 30 microshells in order to quantify the error among the coefficients and their estimation. With 11 radiographs and 7 estimated modes, the variance between the 30 results is very low $\sim 10^{-5}$ mm. The precision decreased significantly when the number of radiographs tends toward the number of estimated modes and if the number of radiographs is lower than the number of the estimated mode, the estimation fails.

When the number of images is greater than the estimated mode, the error on the coefficient is of the order of magnitude of the uniform noise added to the contours during the simulation. On the other hand, if the number of images is too small compared to the estimated modes, it is not possible to reconstruct this mode.

Indeed, although the Nyquist-Shannon sampling theorem does not apply, aliasing may exist [17], and we need a sufficient number of images compared to the order of the mode to correctly estimate each mode.

V. APPLICATIONS

V.A. Taking a radiograph

Radiography conditions play an important role in characterization. The generator set energy, the acquisition time, the position of the different elements, and the type of support chosen have an impact on the quality of the data recorded & their processing.

The choice of the support is important; indeed, the coefficients of the spherical harmonics will be disturbed if part of the microshell contour is missing. The choice of a conical support allows a total edge detection. Absorption is heterogeneous but does not impact edge detection, since the contact between the microshell and the support is minimum.

The support-microshell assembly is positioned on the X-ray bench, in the set of motorized tables. The microshell and the support are aligned with the X-ray beam, close to the micro-focus generator to ensure maximum magnification and thus the largest microshell image possible.

The radiography follows the following procedure: a first radiograph is made by choosing the parameters of acquisitions, namely:

- the accelerating voltage, chosen around 20 keV to have an absorption by plastic material observable on the radiographs,
- an intensity and exposure time that enhances the contrast, that is that increases the number of photons received on the detector during acquisition (usually 30 seconds for an intensity on the generator target of 5 μA).

Radiographs with a regular angular rotation, dependent on the number of shots, are carried out. For example, for 11 shots, the step is 32.7 degrees for the full 360 degrees rotation to collect the entire series of radiographs needed.

The microshell moves slightly from image to image because the theta rotation stage may have runout. To measure the coefficient of magnification, we use a standard[d]. The magnification is known by the position of the microshell, and the size of the microshell can be measured.

In order to identify spherical harmonics coefficients, one point of the microshell must serve as a reference for all images. Since it is not possible to make a reference mark on the microshell,

[d] The selected standard is a sapphire ball of 1002 μm ± 0.5 μm

we assume that the centroid of the inner surface is a fixed point on our images. This hypothesis implies an error that can not be evaluated [e].

V.B. Contour detection

An outline detection is performed on the acquired radiographs. A classical method for edge detection is the application of a Canny filter, without thresholds or with thresholding (see Figure 10(b)). It is noticed that the detection by the Canny filter is noisy and depends strongly on the contrast of the image (itself related to the flux of the generator and the acquisition time of a radiograph). Therefore, this filter is not robust.

To achieve more robust filtering at experimental conditions, two pieces of information about the X-ray microshell are used:

- the radiograph of a microshell is approximately a disk centered on the image;
- the interfaces are defined by an inflection point on the X-ray profiles.

The geometry of the system suggests adopting polar coordinates. This approach implies an accurate estimation of the center position.

To do so, a Gaussian filter is applied, allowing the background noise to be reduced according to the standard deviation σ of the Gaussian. However, this filter may induce a bias that is not quantifiable. Indeed, the Gaussian filter blurs the image by distorting the contours because the convolution between the image and the filter is discrete[f]. So it is a first step and the center will be estimated with accuracy in a future step.

Knowing that the contour is defined by a point of inflection on each profile, a Laplacian filter is applied in order to amplify the contrast (see Figure 10(c)). The variations around the contours make the inflection point more visible. In addition, this filtering is performed in polar coordinates to amplify the variations on the profiles passing through the center of the image.

After filtering, the image is transformed back into Cartesian coordinates. A Canny filter with segmentation gives the contours (see Figure 10(d)). The filter is more robust, as it can be

[e] Indeed, it would be necessary to have a reference, a surface for example. However, the objective of the measurement is the knowledge of the surfaces which is not known a priori. This error is therefore inherent to the method if there is not a way to establish a link between the different relative references of radiograph and an absolute reference for the set of radiographs (and microshell).

[f] Contrary to a continuous convolution which does not move the edge, as shown in section III.B.1.

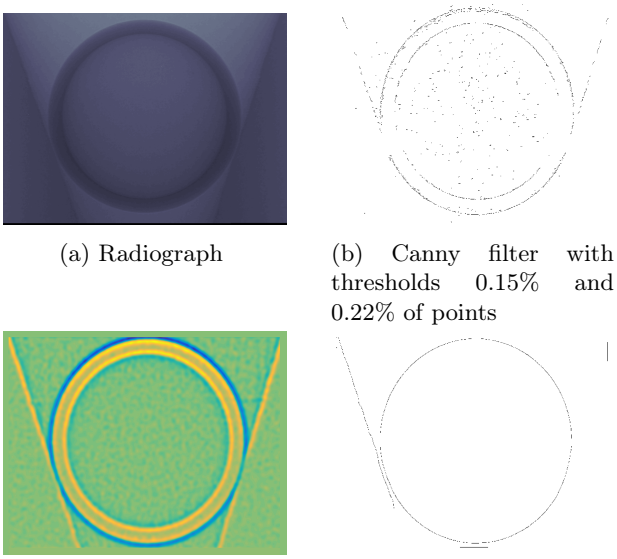

(a) Radiograph

(b) Canny filter with thresholds 0.15% and 0.22% of points

(c) Gaussian filter ($\sigma = 10$ *pixels*) and derivation

(d) Canny filter, after Gaussian filtering and derivation, with thresholds 0.1% and 0.3% of points

Fig. 10. Edge detection.

seen on microshell shots with a different X-ray instruments, for example, a shot taken from X-ray tomography of the same microshell as before (see Figure 11).

Using a Circle Hough Transform [18], a first estimate of the center of the microshell can be found, but the error is still too large (Hough's Transform does not provide a precision less than a pixel). Then, on each profile passing through the previously defined center, a maximum amplitude is computed: it corresponds to the contrast peak observed on the contours.

The inflection points in each profile located at the left of the contrast peak (the center being at the origin) correspond to the border of the microshell and are used for next step.

The P points defining each contour are located for each radiograph (cf. Figure 12).

These points are used in the weighted least-squares method previously presented, to estimate the coefficients of the spherical harmonics (see the values of the coefficients of the first 3 modes for the different surfaces, table I).

We perform a last correction on the estimated center of the microshell. Indeed, mode 1 of the inner surface should be equal to zero since the center of the inner surface has been chosen as the origin. Therefore, we force the mode 1 to zero and transfer the translation to mode 1 of the

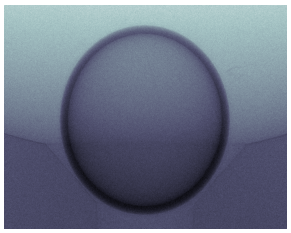

(a) Microshell radiograph on X-rays tomography system

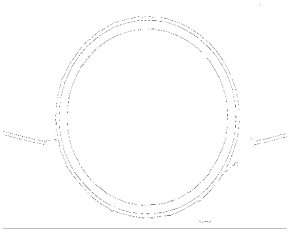

(b) Canny filter, after Gaussian filtering and derivation, with thresholds 0.1% and 0.3% of points

Fig. 11. Edge detection on a radiograph from a tomography system (experimental conditions different from radiography).

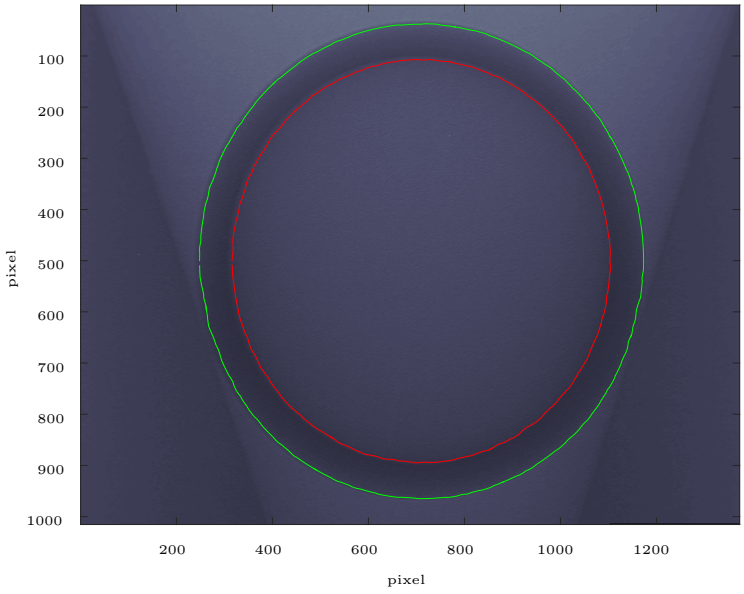

Fig. 12. Radiograph of a polished plastic microshell doped of silicon with an outer diameter of 2230 μm, with the outer and inner contour detected points.

TABLE I
Estimated coefficients $\lambda_{l,m}$ (see (12)) of outer and inner surfaces.

l	m	outer (μm)	inner (μm)
0	0	+1578,137	+1340,433
1	-1	-0,543	+0
1	0	+0,013	+0
1	1	-2,257	+0
2	-2	+0,021	+0,016
2	-1	+0,115	+0,046
2	0	-0,05	-0,023
2	1	+0,013	+0,011
2	2	+0,044	+0,069

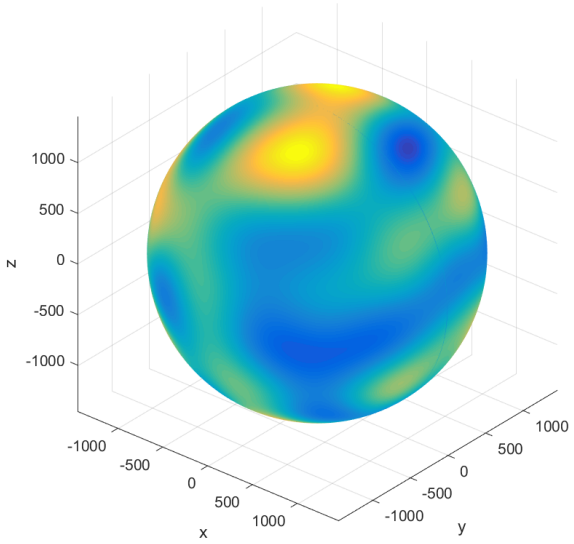

Fig. 13. Measured microshell wall thickness.

outer surface.

These results characterize the surfaces and thicknesses of the microshell, and it is possible to reconstruct the surface of the microshell in 3D as shown in Figure 13.

V.C. Method validation

To validate the method, the same microshell is characterized several times with 7 different initial orientations. The microshell is composed of plastic doped of silicon with a radius of 1115 μm[g]. The mean power and the standard deviation of the 7 measures is given in table II. The results are identical up to a variation about 2 μm.

TABLE II
Mean power $\sqrt{\sum_m \lambda_{l,m}^2}$ and standard deviation of 7 measurements.

	l	mean (μm)	std
inner	0	945.7	1.9
	1	0	0
	2	1.5	0.8
outer	0	1109.8	1.9
	1	5.8	0.6
	2	4.5	1.5
thickness	0	164.2	0.5
	1	3.7	2.5
	2	3.5	0.6

VI. MEASUREMENT UNCERTAINTY

To perform the error analysis, we apply the Guide to the expression of Uncertainty in Measurement (GUM) [19]. Sources of errors include geometry of the system, the distortion of the image, and the variation of the magnification, the standard deviation during measurement and so on. Let us detail.

On a radiograph for a view angle φ, we measure ρ, the distance between the microshell center and a point on a contour, with:

$$\rho(\theta,\varphi) \in [\bar{\rho}(\theta,\varphi) - U, \bar{\rho}(\theta,\varphi) + U]\,; \tag{15}$$

where $\bar{\rho}$ is the true value of the distance, and U is called coverage uncertainty. The coverage uncertainty U takes into accounts multiple parameters: the uncertainty u and a coefficient k depending of N_m, the number of measurements.

[g] this radius is an a priori estimation obtained from another method of characterization.

This uncertainty u is given by:

$$u^2 = C_j^2 + C_q^2 + C_m^2$$

where

- C_j is the correction due to systematic accuracy error,
- C_q is the correction due to quantification error (the resolution of X-ray instrument),
- C_m is the correction linked to the repeatability (standard deviation).

We will discuss these corrections below.

Accuracy error The error of systematic accuracy is obtained by characterizing a measurement standard. If the characterization of this standard with our method gives results in the range of the uncertainty of the standard, then the correction taken into account is the uncertainty of the measurement standard taken from its calibration certificate.

The available sapphire standard is spherical. The uncertainty of this sample is only given for the radius. The assumption that this uncertainty is identical for all modes is done. The correction of the error of accuracy follows a uniform law of uncertainty 0.5 μm.

Quantification error The resolution of the device is the error induced by the measuring device. In the case of an X-ray detector, the size of the pixels, the distortion of the image, and the variation of the magnification are taken into account in this coefficient.

The microshell is an almost spherical object, of medium radius R, contained in a $2R$ side cube centered at the origin. For an identical height $x = R$, the difference of position on the sensor between the point projection in $(-R, 0, R)$ and the point in $(R, 0, R)$ is then:

$$\Delta x = R\left(\frac{d}{a-R} - \frac{d}{a+R}\right)$$

For $R = 1\ mm$, $a = 1\ cm$ and $d = 40\ cm$, $\Delta x = 80\ \mu m$. This error is about 1.5 pixel ($55 \times 55\ \mu m$) on the image intensifier sensor, several pixels ($9 \times 9\ \mu m$) on the digital sensor. The image intensifier sensor has approximately 1000×1000 pixel. The distance from the center of the

microshell to a point on the contour is about half the pixels [h]. The pixel deviation d_r is therefore $\frac{1.5}{500} = 0.003\ pixel = 0.165\ \mu m$. This pixel deviation is considered to be the most important device resolution error. It is assumed that this uncertainty follows a uniform law, the standard uncertainty is then $\frac{d_r}{N_m.2\sqrt{3}}\ \mu m$.

Repeatability The metrology is measured as follows: the acquisition of radiographs and estimation of the spherical harmonics coefficients is repeated several times, with a microshell positioned randomly between each series of shots[i].

Let $\bar{y}$ be the true value (the physical value) of the spherical harmonic deformation coefficients of a microshell surface, and ε the error committed at each measurement. A y measure is $y = \bar{y} + \varepsilon$ and ε is the realization of a random variable with centered normal distribution.

This principle is applied for the X-ray characterization of a microshell. Seven measurements are made to decrease the error (under the assumption that the error follows a Gaussian law) and the results are compared to the expectation of y.

The position of the microshell is not known, so the different rotations that the microshell undergoes during the various measurements imply that the coefficients of the spherical harmonics do not have the same values. In order to compare the results of the different measurements, the power of each mode will be compared and not each coefficient separately. For a l mode of spherical harmonics, the power P_l is defined by:

$$P_l = \sqrt{\sum_{m=-l}^{l} \lambda_{l,m}^2}$$

and should be invariant with respect to rotation in space [20].

The results of this metrology are given in the table II, for 7 first modes and 11 radiographs for each measurement. The variance on all modes is less than 2.5 μm.

In the case of the mean squares applied to spherical harmonics, only the variance between the estimated coefficient powers is known. It is the variance obtained for N_m measurements. It follows a normal law, with the type uncertainty $\frac{\sigma}{\sqrt{N_m}}$. For 7 independent measurements of a microshell,

[h] At the X-ray the maximum magnification is sought, and the microshell is projected on the whole sensor.

[i] In fact, the microshell is removed from the support with a brush and then replaced in its support by having rotated the brush. The microshell rolls and slides on the wall of the support to reach a new position.

the maximum of standard deviation for all the spherical harmonic modes is $\sqrt{0,500}\ \mu m$.

Numerical calculation The uncertainty for 7 measurements is then:

$$u^2 = \frac{0,500}{7} + \left(\frac{0,165}{7 * 2\sqrt{3}}\right)^2 + 0,500^2 = 0,3215\ \mu m.$$

The coverage factor for 7 measurement is $k = 2.45$ (cf. GUM annexes) and then, the coverage uncertainty is:

$$U = ku = 1.3891\ \mu m.$$

The measure of spherical harmonics coefficients is given with a coverage uncertainty of $1.4\ \mu m$, which is in accordance to the expected micrometer accuracy. This uncertainty is the maximal uncertainty on all modes measured.

VII. CONCLUSIONS

The phase contrast is modeled by geometrical optics. Theoretical model of X-ray propagation gives information on particular points on simulated radiograph. These points are used for a shape detection and an estimation of surfaces defects described in spherical harmonics. The uncertainty of the model is given for our radiography system. Improving the quality of the information which can be found from phase contrast, especially on the physical and chemical composition of microshell, is still a work in progress.

VIII. ACKNOWLEDGMENT

This work was partially supported by the SRGI ANR Grant ANR-15-CE40-001. All authors wished to thank Pr. Fulvia Arfelli and Ralf Menk from Elettra Sincrotone Trieste for fruitful discussions.

We would like to thank the reviewer for his/her carreful reading and numerous corrections as well as his/her comments on the manuscript.

REFERENCES

[1] C. Lion, "The LMJ program: An overview.," *Journal of Physics: Conference Series*, vol. 244, no. 1, p. 012003, 2010.

[2] R. Collier, F. Bachelet, R. Botrel, O. Breton, C. Chicanne, C. Dauteuil, F. Durut, E. Fleury, L. Guillot, C. Hermerel, and L. Jeannot, "Target developments program to prepare LMJ campaigns," *Journal of Physics: Conference Series*, vol. 244, no. 3, p. 032037, 2010.

[3] A. Choux, E. Busvelle, J. P. Gauthier, and G. Pascal, "Observer for a thick layer of solid deuterium-tritium using backlit optical shadowgraphy and interferometry," *Applied optics*, vol. 46, no. 33, pp. 8193–8201, 2007.

[4] A. Choux, R. Garrot, G. Geoffray, C. Hermerel, L. Jeannot, and O. Legaie, "Quantitative dimension measurement of laser target composents using hamamatsu microfocus source," *Digital Industrial Radiology And Computed Tomography, june 20–22, 2011, Berlin, Germany*, 2011.

[5] A. Choux, L. Barnouin, L. Reverdy, and M. Theobald, "Characterization of microshells experimented on laser megajoule using x-ray tomography," *7th Industrial Computed Tomography, february 06–09, 2017, Leuven, Belgium*, 2017.

[6] A. Choux, L. Barnouin, L. Reverdy, and M. Theobald, "Characterization of laser megajoule targets by x-ray tomography," *Fusion Science and Technology*, pp. 1–5, 2018.

[7] B. J. Kozioziemski, J. A. Koch, A. Barthy, and H. E. Martz, "Quantitative characterization of inertial confinement fusion capsules using phase contrast enhanced x-ray imaging," *Journal of applied physics*, 2015.

[8] S. Wilkins, T. Gureyev, D. Gao, A. Pogany, and A. Stevenson, "Phase-contrast imaging using polychromatic hard x-rays," *Letters to nature, volume 384*, 1996.

[9] E. Hobson, *The Theory of Spherical and Ellipsoidal Harmonics (Chelsea, New York, 1965)*. Cambridge University Press, 1931.

[10] H. Groemer, *Geometric applications of Fourier series and spherical harmonics*, vol. 61. Cambridge University Press, 1996.

[11] E. Y. Sidky, C.-M. Kao, and X. Pan, "Accurate image reconstruction from few-views and limited-angle data in divergent-beam ct," *Journal of X-ray Science and Technology*, vol. 14, no. 2, pp. 119–139, 2006.

[12] V. Dutto, *Mesure des défauts de forme de microballons par imagerie X : exploitation du phénomène de contraste de phase*. PhD thesis, Université de Toulon, 2018.

[13] A. Choux, *Commande optimale d'un système de conformation cryogénique d'une couche solide d'isotope de l'hydrogène dans un microballon par chauffage infrarouge*. PhD thesis, Université de Bourgogne, 2006.

[14] B. L. Henke, E. M. Gullikson, and J. C. Davis, "X-ray interactions: photoabsorption, scattering, transmission, and reflection at e= 50-30,000 ev, z= 1-92," *Atomic data and nuclear data tables*, vol. 54, no. 2, pp. 181–342, 1993.

[15] M. Guillaume, *Analysis and synthesis of sound field*. PhD thesis, Télécom ParisTech, 2006.

[16] P. Keegstra, C. Bennett, G. Smoot, K. Gorski, G. Hinshaw, and L. Tenorio, "Generalized spherical harmonics for all-sky polarization studies," *Astronomical Data Analysis Software and Systems*, vol. 125, 1997.

[17] T. Li and G. North, "Aliasing effects and sampling theorems of spherical random fields when sampled on finite grid," *Ann. Inst. Statist. Math.*, vol. 49, no. 2, pp. 341–354, 1997.

[18] T. J. Atherton and D. J. Kerbyson, "Size invariant circle detection," *Image and Vision computing*, vol. 17, no. 11, pp. 795–803, 1999.

[19] BIPM, *Guide to the expression of uncertainty in measurement*. Joint Committee for Guides in Metrology, 2008.

[20] M. Kazhdan, T. Funkhouser, and S. Rusinkiewicz, "Rotation invariant spherical harmonic representation of 3 d shape descriptors," in *Symposium on geometry processing*, vol. 6, pp. 156–164, 2003.